Geophysical Research Letters

RESEARCH LETTER
10.1029/2025GL114640

Length Scales, Rates, and Variability of Mixing Downstream of River Confluences

Tasneem Haq Meem[1], Bruce L. Rhoads[1], Quinn W. Lewis[2], Muhammad Umar[1], and Alexander Sukhodolov[3]

[1]Department of Geography and Geographic Information Science, University of Illinois at Urbana-Champaign, Urbana, IL, USA, [2]Headwaters Corporation, Lakewood, CO, USA, [3]Liebnitz Institute of Freshwater Ecology and Inland Fisheries, Berlin, Germany

Key Points:

- The average length scale for complete mixing, which occurred for 45% of 150 events, is 7.4 times the downstream flow width
- On average mixing exhibits a non-linear spatial pattern, conforming with relationships predicted from shallow flow theory
- Mixing rates are highest immediately downstream of confluences and 80% of fully mixed events occur within 15 flow widths of confluences

Supporting Information:

Supporting Information may be found in the online version of this article.

Correspondence to:

T. H. Meem,
tmeem2@illinois.edu

Citation:

Meem, T. H., Rhoads, B. L., Lewis, Q. W., Umar, M., & Sukhodolov, A. (2025). Length scales, rates, and variability of mixing downstream of river confluences. *Geophysical Research Letters*, *52*, e2025GL114640. https://doi.org/10.1029/2025GL114640

Received 10 JAN 2025
Accepted 20 MAR 2025

Abstract Past work on lateral mixing downstream of river confluences has focused on mixing at individual confluences, limiting general knowledge of this process. This study evaluates the average length scales, rates, and variability of lateral mixing downstream at 43 confluences for 150 events based on contrasts in gray-scale intensity of confluent flows captured by aerial images. Only 45% of the events exhibit complete mixing over the length of the imaged downstream reach. The average dimensionless length scale (s_d) of complete mixing is 7.4 times the downstream flow width and varies from s_d = 1.1–26.3, but not all flows completely mix. A nonlinear spatial pattern of mixing, consistent with relations derived from shallow flow theory, reveals that mixing rates are substantially higher immediately downstream of confluences with most mixing occurring over $s_d < 15$. The findings confirm that confluences are important locations of accelerated mixing in river networks.

Plain Language Summary When two rivers flow into each other they start to mix. Understanding mixing downstream of confluences is important for determining the dispersal of water-transported materials, including pollutants, within river systems. Past work has focused mainly on mixing at individual confluences, limiting general knowledge of the mixing process. This study assesses amounts of mixing, the average length of complete mixing, and mixing rates for 150 events at 43 confluences based on contrasts between the two flows visible on aerial photographs. Results indicate that in 45% of the events, the two flows mix completely over the length of river captured on aerial images. In these cases, the average length for complete mixing is 7.4 times the width of the river downstream of a confluence. The pattern of mixing over distance is nonlinear with rapid mixing near the confluence and reduced mixing far from the confluence. Most mixing (≈80%) occurs within 15 times the width of the river downstream of a confluence. The findings confirm that confluences are important locations for enhanced river mixing.

1. Introduction

Confluences are important locations in drainage networks where rivers flow into one another, initiating lateral mixing (Rhoads, 2020). Highly turbulent, three-dimensional patterns of fluid motion at and immediately downstream of confluences (Boyer et al., 2006; De Serres et al., 1999; Duguay et al., 2022; Horna-Munoz et al., 2020; Lyubimova et al., 2021; Pouchoulin et al., 2020; Rhoads & Sukhodolov, 2001; Sukhodolov et al., 2017; Sukhodolov & Rhoads, 2001; Sukhodolov & Sukhodolova, 2019; van Rooijen et al., 2020; Zhang et al., 2020)—a region referred to as the confluence hydrodynamic zone (CHZ) (Kenworthy & Rhoads, 1995)—can potentially increase rates of mixing by enhancing advective and diffusive processes that govern mixing (Sukhodolov et al., 2023). These processes are influenced by a variety of confluence characteristics including the momentum ratio, discharge ratio, velocity ratio, and density ratio of incoming flows, junction angle, and bed morphology (Rhoads, 2020). Despite recognition of confluences as important mixing zones in river systems, clear evidence of a general tendency for enhanced mixing at confluences is lacking. Field studies have mainly involved detailed investigations of mixing at and downstream of individual confluences. Some studies report rapid mixing (Gaudet & Roy, 1995; Lane et al., 2008; Lewis & Rhoads, 2015; Lewis et al., 2020), whereas others have documented limited mixing over long distances downstream of confluences (Bouchez et al., 2010; Campodonico et al., 2015; MacKay, 1970; Matsui et al., 1976; Stallard, 1987). Large contrasts in momentum flux and density between incoming flows seem to contribute to rapid mixing (Horna-Munoz et al., 2020; Lewis et al., 2020).

To date, no studies have examined mixing downstream of a large number of confluences, partly because field investigations of confluences are time-consuming and costly. Thus, little is known about characteristic rates and

length scales of this type of mixing. Alternatively, remote-sensing data from airborne or satellite platforms can be used to assess spatial rates and patterns of mixing at many confluences at low cost (Umar et al., 2018). Knowledge of mixing rates and length scales downstream of confluences is important for determining spatial scales of mixing within river networks (Launay et al., 2015; Wang et al., 2024). It also informs concerns about water quality and aquatic habitat of river systems (Gooseff et al., 2008; Kiffney et al., 2006; Tavernini & Richardson, 2020; Yuan et al., 2022). From a practical perspective, mixing of confluent flows is a vital consideration in the dispersal of riverine pollutants (Tang et al., 2018; Zhang et al., 2020, 2023). Here we examine spatial scales and rates of mixing downstream of confluences based on contrasts in turbidity on aerial images for 150 mixing events at 43 river confluences across the USA. Our results provide insight into spatial variability in average length scales and rates of mixing downstream of confluences, variability in these rates and length scales, and the frequency of complete mixing over specific downstream length scales.

2. Methods

An established confluence mixing-metric procedure (Umar et al., 2018) developed for satellite remote-sensing data was adapted to analyze spectral information obtained from aerial photographs (Figure S1 in Supporting Information S1). The procedure employs a grid-based measurement scheme to characterize spatial variation in 8-bit gray-scale pixel values (0–255) downstream of confluences, averages pixel values to determine lateral variation in these mean values at discrete cross sections within the grid, computes a standardized mixing metric for each cross section based on lateral variation in mean pixel values, and assesses change in the mixing metric over distance downstream of the confluences.

2.1. Data

Gray-scale data on confluence mixing were derived from high-resolution (<2 m pixels) orthorectified color (RGB) aerial images (National Agriculture Imagery Program—NAIP) obtained between 2002 and 2020 as part of the National Agricultural Imagery Program (NAIP). Individual digital images were downloaded using Google Earth Engine. The data set consists of 150 mixing events at 43 confluences from throughout the United States (Table S1 in Supporting Information S1). All events exhibit a distinct contrast in turbidity between the confluent rivers. River size based on flow width downstream of the confluences ranges from 45 to 535 m with an average of 147 m.

Although NAIP images are obtained from an aerial camera, and are not corrected for radiometric or atmospheric effects, image processing conforms to rigorous standards for balanced tone, contrast, brightness, and color, thereby providing a high degree of consistency in gray-scale intensity information (Bunis, 2007). Evaluations of pixel-value uniformity were conducted to ensure consistency of gray-scale information on this imagery (Supporting Information S1). This evaluation indicated that inherent variability in gray-scale pixel values for areas of relatively uniform river turbidity upstream of confluences is, on average, an order of magnitude less than the variability in pixel values associated with contrasts in turbidity between confluent flows. These evaluations confirm that noise levels in pixel values are small relative to the signal produced by contrasts in turbidity.

2.2. Data Processing

River edges of water downstream of each confluence were manually digitized in ArcGIS Pro 3.0 for each aerial image to produce boundary polygons that consist entirely of water pixels. Manual digitization was necessary to avoid inclusion of overhanging vegetation, shadows, bars, and bank irregularities that can affect spectral characteristics near channel banks. The centerline of the downstream river was determined using the "Collapse Dual Lines to Centerline" tool in ArcGIS based on the digitized edges of water. Geographic coordinates of each pixel within the boundary polygon were extracted from each aerial photo and these coordinates were transformed into stream-wise (s—parallel to centerline) and lateral (n—perpendicular to centerline) coordinates, where $s = 0$ corresponds to the upstream junction corner and $n = 0$ corresponds to the centerline (Figure S2 in Supporting Information S1). The gray-scale value for the red or green band was extracted for each pixel; the red band generally produced the greatest contrast in gray-scale values between the two confluent flows, but in a few cases the green band had the highest contrast.

Spatial averaging was performed to reduce noise associated with individual pixel values (Figure S2 in Supporting Information S1). Cross sections (CS) oriented perpendicular to the channel centerline were defined at discrete

locations along the downstream channels and pixel values were averaged within longitudinal segments of the channels centered on the cross sections. Spacings of the cross sections, which ranged from $s_d = 0.06$–0.45 [$s_d = s/W$, where s is distance (m) and W is flow width (m)], varied depending on channel width and change in direction of the channel (to avoid intersection of cross sections). Each longitudinal segment was divided into subsegments ($\Delta s = 4$ m) in the streamwise direction (Figure S2 in Supporting Information S1). The n coordinates of pixels (n_i) were normalized (n_d) based on the width of the Δs subsegments relative to the CS width:

$$n_d = n_i * \frac{\text{width of CS}}{\text{local width of subsegment}} \quad (1)$$

Each longitudinal segment was divided laterally into bins ($\Delta n = 3$ m). Gray-scale values associated with all pixels within the bins along the length of each subsegment were then averaged. These mean pixel values (S_i) were assigned to bin centroids (Δn) on each cross section within the downstream reach (Figure S2 in Supporting Information S1).

2.3. Mixing Metric

The amount of mixing of the confluent flow was determined using a mixing metric (P_{mx}) that compares the standard deviation of S_i values at cross sections downstream of a confluence, corrected for inherent variability of S_i values, to the standard deviation of S_i values at a composite cross section of the two incoming flows upstream of the confluence (Umar et al., 2018) (Equation S3 in Supporting Information S1). The value of P_{mx} ranges from 0 to 1 with zero indicating no mixing and, similar to previous studies (Rutherford, 1994), $P_{\text{mx}} \geq 0.95$ considered complete mixing. In all cases, variability in pixel values related to contrasts in turbidity between the two flows upstream of the confluence greatly exceeded inherent variability in pixel values for relatively uniform turbidity within each incoming flow. In other words, inherent variability in pixel values, which reflects noise in gray-scale information, was much less than the variability caused by contrasts in turbidity between the incoming flows. The mixing metric assumes that mixing is conservative, that is, that changes in gray-scale values downstream of a confluence are related to combining of the two flows without losses or additions of material suspended in the flow; thus, changes in mean gray-scale values in the downstream channel represent mixing of two incoming flows with spatially invariant gray-scale characteristics. Determining whether mixing is purely conservative is difficult to ascertain from imagery only and could not be verified for the cases analyzed in this study. Care was taken to avoid obvious situations where the assumption is violated, such as additions of tributary flow downstream of a confluence. Local sources of gray-scale noise can also affect the mixing metric, resulting in P_{mx} values much less than 0 and much greater than 1. Cross sections that include such sources, including bridges, bars, or unusual variations in water tone, were excluded from analysis of change in P_{mx} over distance. Finally, the methodology and metric adopted here only considers the surface character of mixing and cannot account for mixing that is not visible at the surface, such as subsurface effects related to strong secondary currents (Lewis et al., 2020) and density contrasts (Horna-Munoz et al., 2020).

3. Results

3.1. Quantifying and Mapping Lateral Mixing Downstream of Confluences

Examples of mixing events show how spatial variations in mean gray-scale values of aerial images define spatial patterns of mixing downstream at confluences both across the channel and along the downstream channel (Figure 1). In all events, marked contrasts in turbidity produce tonal differences between the two confluent flows, resulting in pronounced lateral variation in S_i at cross sections downstream of the confluences. Patterns of lateral variation in S_i exhibit a characteristic S shape (Umar et al., 2018) that, based on theoretical considerations (Equation S1 in Supporting Information S1) (Sukhodolov et al., 2010), are approximated by hyperbolic tangent functions (Equation S2 and Table S2 in Supporting Information S1, Figure 1). For the first case (Figure 1a), the lateral variation in S_i rapidly diminishes downstream. Complete mixing ($P_{\text{mx}} \geq 0.95$) occurs rapidly over a streamwise dimensionless distance of only $s_d = 1.8$. For the second case (Figure 1b), the lateral variation in S_i decreases gradually over the length of the channel. Mixing occurs relatively slowly but reaches $P_{\text{mx}} \geq 0.95$ at $s_d = 11$ (CS 28). In the third event (Figure 1c), initially strong lateral variation in S_i diminishes slightly over distance but persists over the downstream extent of the channel.

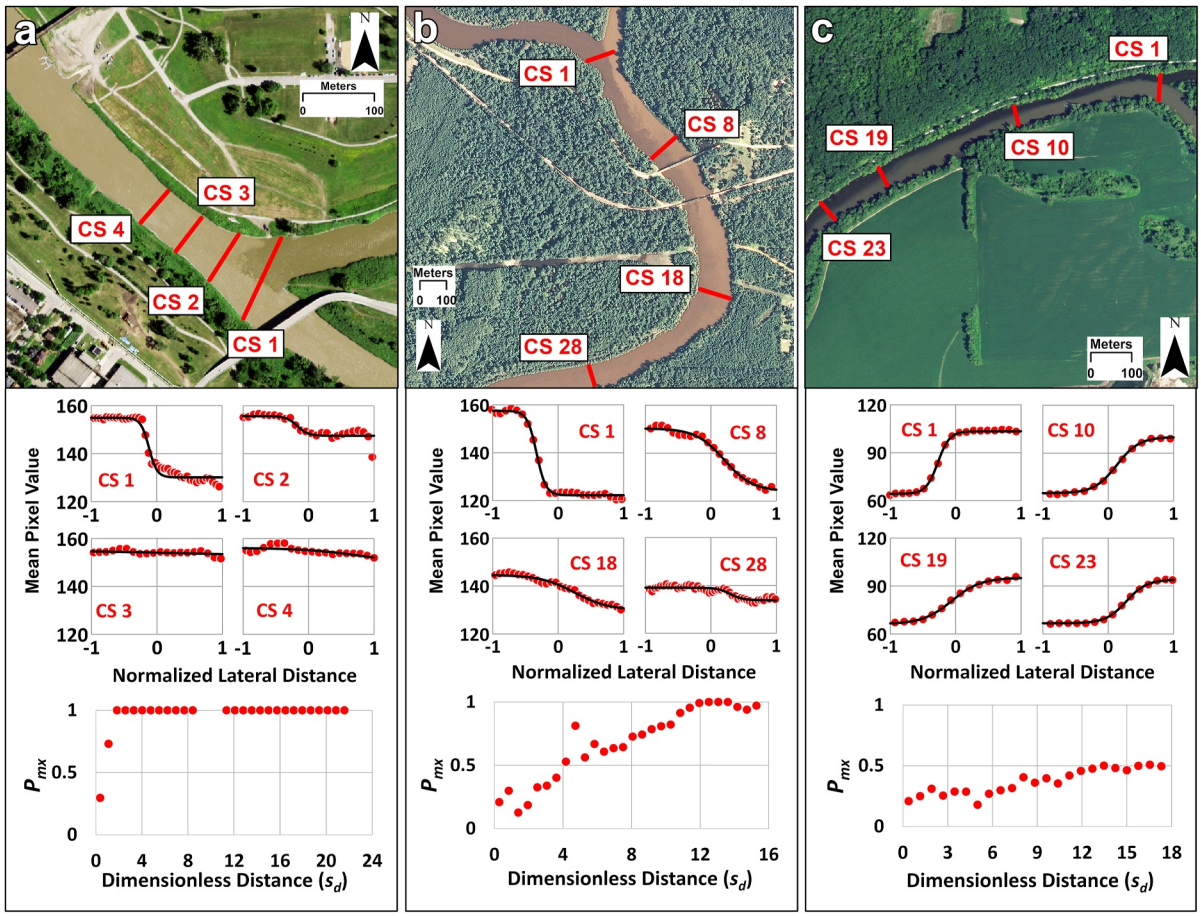

Figure 1. Examples of spatial patterns of mixing downstream of confluences: aerial photos of (a) confluence of Red Lake River and Red River of the North in Minnesota (23 July 2018), (b) confluence of Leaf River and Pascagoula River in Mississippi (9 September 2012), and (c) confluence of Grand River and Maple River in Michigan (27 July 2016). Four cross sections (CS) downstream of each confluence are indicated as red lines along with labels specifying cross-section numbers. Below each photo (a–c): top plot shows mean pixel values (S_i) versus normalized lateral distance (n_d) at the four cross sections on each aerial photo with black lines corresponding to hyperbolic tangent functions fit to the patterns of reflectance data; bottom plot illustrates change in fractional mixing (P_{mx}) over dimensionless distance downstream of the confluences (s_d).

The value of $P_{mx} \approx 0.5$ at $s_d = 17$ (CS 23) substantiates that the two flows are only partially mixed at the downstream end of the reach on the image.

3.2. Distribution of Complete Mixing and Partial Mixing: Frequency Versus Dimensionless Distance

The cumulative frequency distribution of 150 mixing events reveals that complete mixing ($P_{mx} \geq 0.95$) occurred in 67 events, or 45% of all events (Figure 2a). Conversely, the two flows are partially mixed ($P_{mx} < 0.95$) for the remaining 83 events (55%). Only five of the 150 events (3.3%) exhibit full mixing within $s_d = 2$ and the rate of increase in the percentage of fully mixed events is greatest between $2 < s_d < 8$. Seventy percent of events with full mixing are located at or upstream of $s_d = 8$. The rate of increase in fully mixed cases diminishes over $8 < s_d < 14$ with 94% of the fully mixed cases occurring at or upstream of $s_d = 14$. For $s_d > 14$, only four of the 67 events (6%) with complete mixing become fully mixed. One hundred percent of events with full mixing occur at or upstream of $s_d = 26.5$.

3.3. Length Scale of Mixing

For events with complete mixing, the average dimensionless length scale of this mixing ($\overline{L_m}$) is 7.4. At and upstream of this dimensionless distance 41 of the 67 fully mixed cases (61%) exhibit complete mixing (Figure 2b). The average dimensionless length of downstream reaches visible on individual aerial images ($\overline{L_r}$) for events with

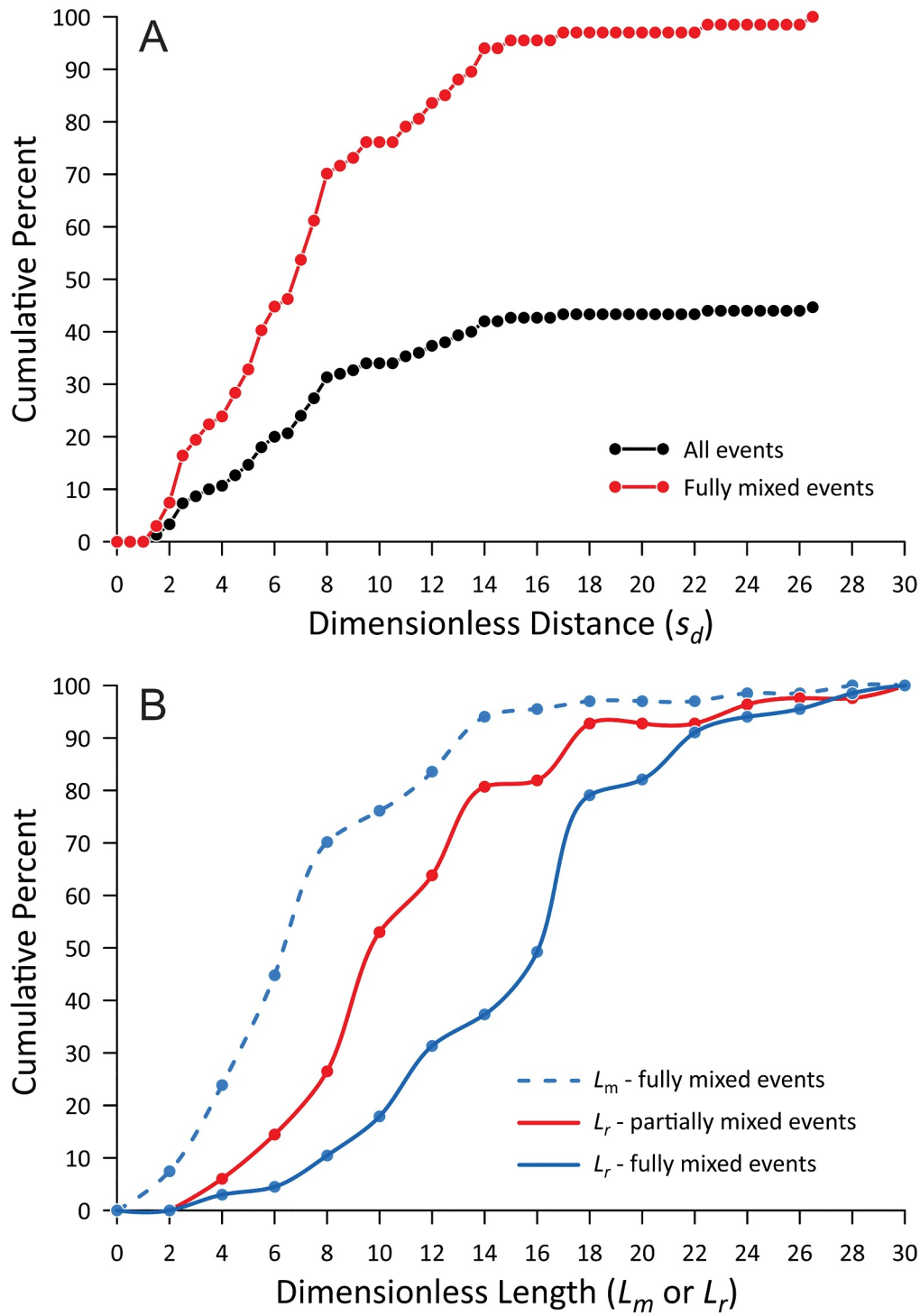

Figure 2. (a) Cumulative percent of events with complete mixing at different dimensionless distances downstream from confluences for all 150 events (black) and for completely mixed events only (red). (b) Cumulative distributions of dimensionless mixing lengths (L_m) and downstream reach lengths (L_r) for fully mixed events and reach lengths (L_r) for partially mixed events.

complete mixing is 15.3 so that, on average, complete mixing occurs over about half of this distance. Individual values of mixing length (L_m) vary over an order of magnitude (1.1–26.3) with a standard deviation (σ_m) of 4.9. The coefficient of variation $\left(\sigma_m/\overline{L_m}\right)$ is less than one (0.66), signifying relatively low variability of individual events

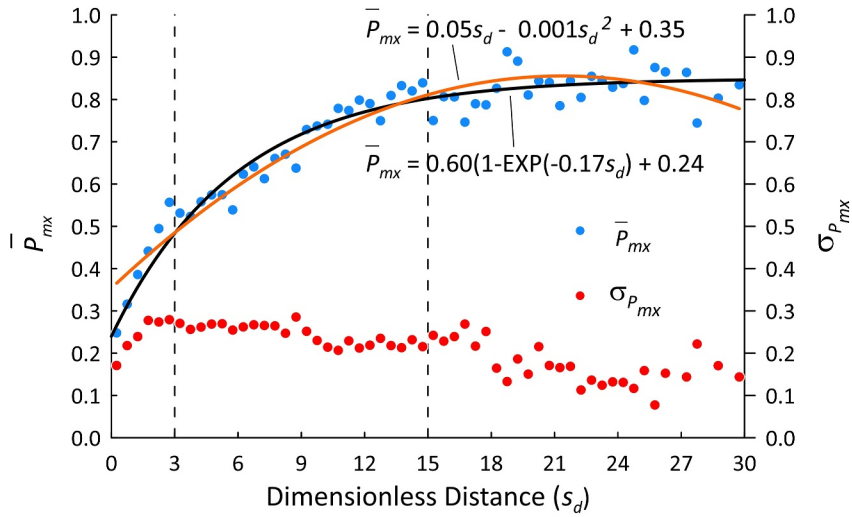

Figure 3. Spatial pattern of $\overline{P}_{\mathrm{mx}}$ versus s_d and of $\sigma_{P_{\mathrm{mx}}}$ versus s_d for all 150 events, including exponential (black, SE = 0.04) and polynomial (orange, SE = 0.04) functions fit to the data (SE = standard error). Dashed vertical lines indicate segmentation of the nonlinear pattern of the $\overline{P}_{\mathrm{mx}}$ data into three distinct linear domains.

in relation to $\overline{L_m}$. The median value of L_m (6.9) is less than $\overline{L_m}$ (7.4), reflecting positive skewness of the distribution of complete mixing lengths (Figure 2b).

For events with partial mixing, $\overline{L_r}$ = 11.3, which exceeds $\overline{L_m}$ = 7.4 for events with complete mixing. Overall, values of L_m are less than values of L_r for events with partial mixing, even though values of L_r for events with complete mixing exceed values of L_r for partial mixing (Figure 2b). Thus, the lack of complete mixing for partially mixed events cannot be attributed to short lengths of downstream reaches; instead, these events tend to mix less rapidly than the complete mixing events. Differences in L_r among the various events are the inevitable outcome of utilizing single aerial images of the confluences, which contributed to consistency in spectral characteristics required to rigorously quantify mixing patterns.

Average flow widths for complete versus partial mixing events are 123 and 180 m, respectively, implying that mixing tends to occur over longer distances in wider rivers. This result is consistent with basic considerations of mixing downstream of confluences derived from river mixing theory, which predicts that $L_m \propto W^2$ (Bouchez et al., 2010, 2011). According to this relation, $\overline{L_m}$ for partial mixing cases should be about 2 times $\overline{L_m}$ for complete mixing cases (≈15), which exceeds $\overline{L_r}$ for the partial mixing cases (≈11).

3.4. Mixing Rates and Variability of Mixing Rates

A plot of $\overline{P}_{\mathrm{mx}}$ versus s_d for all 150 mixing events, where values of $\overline{P}_{\mathrm{mx}}$ equal averages of all P_{mx} data within successive s_d intervals of 0.5, reveals a nonlinear spatial pattern of mixing characterized by relatively rapid mixing close to the confluence and a gradual decrease in the rate of mixing over distance (Figure 3). The spatial pattern of $\overline{P}_{\mathrm{mx}}$ generally conforms both to polynomial and exponential relations for lateral increase in mixing-interface width derived from two-dimensional shallow flow equations based on consideration of lateral advective and turbulent fluxes of momentum, bed friction and pressure difference terms (Equations S4–S7 in Supporting Information S1, Figure 3) (Sukhodolov et al., 2023). The data indicate that confluent flows tend to mix on average by approximately 80%–90% over s_d = 30. Standard deviations of P_{mx} for each bin ($\sigma_{P_{\mathrm{mx}}}$), which highlight variability in mixing, range from 0.08 to 0.29 with a standard deviation for all bins of 0.05, indicating relative consistency in the variability of mixing over distance (Figure 3). The spatial pattern of $\sigma_{P_{\mathrm{mx}}}$ does not exhibit a uniform spatial trend, but values systematically increase within about 2–3s_d of the confluences and then generally decline somewhat and become more variable as s_d increases.

Although the general spatial pattern of $\overline{P}_{\mathrm{mx}}$ can be characterized using nonlinear relations, close inspection of the data reveals three distinct linear segments of spatial rate of change separated by breakpoints at s_d = 3 and s_d = 15

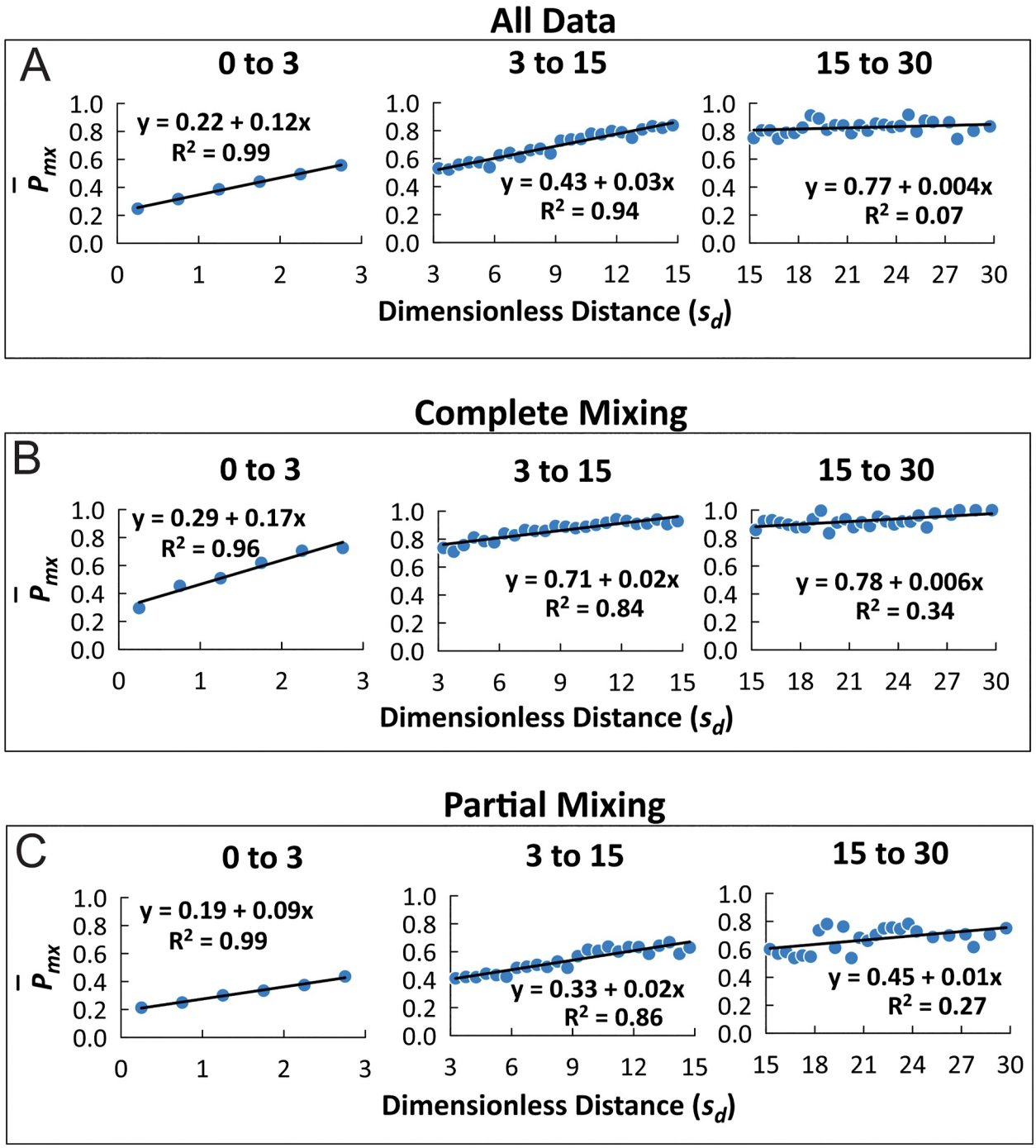

Figure 4. Linear relations (lines) fit to data (blue dots) on plots of dimensionless distance versus the mixing metric for all 150 cases (a), for cases with complete mixing (b) and cases with partial mixing (c).

(Figures 3 and 4a). The greatest linear rate of increase and lowest degree of scatter in $\overline{P}_{\mathrm{mx}}$ occurs for $0 < s_d < 3$. On average, mixing increases by $12\%/s_d$, or about 36%, within this segment, which reflects mixing closest to the confluence. Between $3 < s_d < 15$, the spatial pattern is highly linear, but the rate of increase in mixing per unit width is much less than in the first downstream segment, decreasing to $3\%/s_d$. Over this segment, which is four times longer than the first segment, the total average increase in mixing is similar to that in the first segment (≈36%). In the third segment, which extends from $15 < s_d < 30$, the linear relationship between $\overline{P}_{\mathrm{mx}}$ and s_d is weak and rather poorly defined, but slightly positive, corresponding to an increase in mixing of $0.4\%/s_d$. Overall,

mixing mostly occurs within $0 < s_d < 15$ of the confluences and mixing rates are substantially higher immediately downstream of confluences ($0 < s_d < 3$), where mixing is about four times faster than in the second segment and 30 times faster than in the third segment.

Partitioning the data confirms that mixing rates are higher for complete mixing events versus partial mixing events (Figures 4b and 4c). For complete mixing events, the rate of increase in mixing at $s_d = 0$–3 ($17\%/s_d$) is about 40% greater than for all events ($12\%/s_d$) and nearly double the rate of increase for partial-mixing events ($9\%/s_d$). The increase in the rate of mixing in this first segment for complete-mixing events is approximately 9 times and 28 times faster than that occurring in the second and the third segments, respectively. For partial mixing events, relatively similar increases in mixing occur in the second and third segments (~2% and 1%, respectively).

4. Discussion and Conclusion

Our results generally indicate that spatial rates of mixing downstream of confluences are highest near the confluence apex and diminish over distance. The nonlinear spatial pattern of mixing downstream of confluences is consistent with experimental data that predict an initial rapid increase in mixing over distance followed by a gradual decrease in the spatial rate of mixing (Biron et al., 2004; Sukhodolov et al., 2023; Zhang et al., 2020). The spatial pattern of mixing generally conforms to exponential or polynomial relations derived theoretically from the two-dimensional shallow water equations for open-channel flow (Equations S3 and S4 in Supporting Information S1) that consider the effects of friction, turbulent diffusion, and lateral advection of momentum on mixing downstream of confluences (Sukhodolov et al., 2023). Thus, the results based on a large number of field cases provide confirmation of the general spatial pattern of mixing derived from experimental and theoretical work.

Decomposition of the nonlinear relations into three distinct domains of linear relations highlights the influence of mixing near confluences on the overall spatial pattern of mixing. The first domain ($s_d = 0$–3) clearly occurs within the CHZ. High spatial rates of mixing for this domain are expected given that many mechanisms within confluences can enhance mixing, including advective processes associated with curvature-induced secondary flow (Lewis & Rhoads, 2015; Lewis et al., 2020; Rhoads & Kenworthy, 1995), turbulent diffusive processes generated by Kelvin-Helmholtz and wake-like coherent structures (Constantinescu et al., 2011, 2012, 2014; Lewis & Rhoads, 2015), turbulence and secondary flow related to bed discordance (Biron et al., 1996, 2004; Sukhodolov et al., 2017), and secondary flow produced by density effects (Duguay et al., 2022, 2023; Horna-Munoz et al., 2020; Lyubimova et al., 2021; Ramon et al., 2014). The second domain (s_d = 3–15) appears to represent a transition between the influence of confluence hydrodynamics on mixing and locations where the flow downstream is no longer affected by these complex hydrodynamic conditions. The spatial extent of the CHZ will vary from confluence to confluence as well as at the same confluence as hydrological conditions change over time (Lewis et al., 2020). Moreover, hydrodynamic conditions generated within the confluence will generally decay downstream as distance from local generative mechanisms within the confluence increases (Sukhodolov et al., 2023). Together these effects produce a transitional zone in which enhanced mixing occurs but is less effective than immediately downstream from confluences. The third domain ($s_d = 15$–30) likely signals control of mixing by diffusive and advective processes related to the influence of characteristics of the downstream channel on the flow, rather than to hydrodynamic conditions generated at the upstream confluence. These characteristics include factors such as bed roughness, cross-section geometry, and channel planform. Within this domain, theoretical considerations about river mixing in the absence of confluence effects likely apply (Rutherford, 1994). If hydrodynamic conditions within a confluence do not enhance mixing rates locally to a level that promotes complete mixing a relatively short distance ($s_d < 30$) downstream, the low rates of mixing beyond the influence of the confluence may lead to large increases in the length scale required for complete mixing. Overall, the findings of this study emphasize the importance of confluences as loci of mixing within river systems.

The generalizations derived from the analysis apply to average conditions; individual events exhibit considerable variability in mixing (Figure 1). The occurrence of complete and partial mixing over various length scales is consistent with past work at individual confluences, which has documented both rapid (Gaudet & Roy, 1995; Kenworthy & Rhoads, 1995; Lane et al., 2008; Lewis & Rhoads, 2015; Lewis et al., 2020) and slow (Bouchez et al., 2010; Lane et al., 2008; Laraque et al., 2009; MacKay, 1970; Umar et al., 2018) mixing. The considerable variability in the degree of mixing at any given dimensionless distance downstream indicates that the spatial pattern of mixing at individual confluences can deviate substantially from the relation defined by averaging data for all confluences. Determining the factors that produce different spatial patterns of mixing requires further

investigation. Studies integrating remote sensing, field investigations, and numerical modeling also are needed to evaluate the extent to which remote-sensing data accurately represent mixing at and downstream of confluences, to relate surface mixing patterns to mixing throughout the water column, and to determine the extent to which mixing downstream of confluences is a conservative process.

Data Availability Statement

Data is available at the Illinois Data Bank (Meem et al., 2025).

Acknowledgments
Financial support for TM and BR was provided by the U.S. National Science Foundation Grant EAR-2012850 for the project CINET: Critical Interface Network in Intensively Managed Landscapes. AS acknowledges the financial support from the Deutsche Forschungsgemainschaft (DFG, Grant SU 405/11-1).

References

Biron, P., Best, J. L., & Roy, A. G. (1996). Effects of bed discordance on flow dynamics at open channel confluences. *Journal of Hydraulic Engineering*, *122*(12), 676–682. https://doi.org/10.1061/(asce)0733-9429(1996)122:12(676)

Biron, P. M., Ramamurthy, A. S., & Han, S. (2004). Three-dimensional numerical modeling of mixing at river confluences. *Journal of Hydraulic Engineering*, *130*(3), 243–253. https://doi.org/10.1061/(ASCE)0733-9429(2004)130:3(243)

Bouchez, J., Lajeunesse, E., Gaillarde, J., France-Lanord, C., Dutra-Maia, P., Maurice, L., & Gualtieri, C. (2011). Turbulent mixing in the Amazon River: The isotopic memory of confluences. *Earth and Planetary Science Letters*, *311*(3–4), 448–450. https://doi.org/10.1016/j.epsl.2011.09.049

Bouchez, J., Lajeunesse, E., Gaillardet, J., France-Lanord, C., Dutra-Maia, P., & Maurice, L. (2010). Turbulent mixing in the Amazon River: The isotopic memory of confluences. *Earth and Planetary Science Letters*, *290*(1–2), 37–43. https://doi.org/10.1016/j.epsl.2009.11.054

Boyer, C., Roy, A. G., & Best, J. L. (2006). Dynamics of a river channel confluence with discordant beds: Flow turbulence, bed load sediment transport, and bed morphology. *Journal of Geophysical Research*, *111*(F4), F04007. https://doi.org/10.1029/2005JF000458

Bunis, L. (2007). Aerial photography field office-National Agriculture Imagery Program (NAIP) suggested best practices - final report. ITT Space Systems. Retrieved from https://www.fsa.usda.gov/Internet/FSA_File/naip_best_practice.pdf

Campodonico, V. A., García, M. G., & Pasquini, A. I. (2015). The dissolved chemical and isotopic signature downflow the confluence of two large rivers: The case of the Parana and Paraguay rivers. *Journal of Hydrology*, *528*, 161–176. https://doi.org/10.1016/j.jhydrol.2015.06.027

Constantinescu, G., Miyawaki, S., Rhoads, B., & Sukhodolov, A. (2012). Numerical analysis of the effect of momentum ratio on the dynamics and sediment-entrainment capacity of coherent flow structures at a stream confluence. *Journal of Geophysical Research*, *117*(F4), F04028. https://doi.org/10.1029/2012jf002452

Constantinescu, G., Miyawaki, S., Rhoads, B., & Sukhodolov, A. (2014). Numerical evaluation of the effects of planform geometry and inflow conditions on flow, turbulence structure, and bed shear velocity at a stream confluence with a concordant bed. *Journal of Geophysical Research-Earth Surface*, *119*(10), 2079–2097. https://doi.org/10.1002/2014jf003244

Constantinescu, G., Miyawaki, S., Rhoads, B., Sukhodolov, A., & Kirkil, G. (2011). Structure of turbulent flow at a river confluence with momentum and velocity ratios close to 1: Insight provided by an eddy-resolving numerical simulation. *Water Resources Research*, *47*(5). https://doi.org/10.1029/2010wr010018

De Serres, B., Roy, A. G., Biron, P. M., & Best, J. L. (1999). Three-dimensional structure of flow at a confluence of river channels with discordant beds. *Geomorphology*, *26*(4), 313–335. https://doi.org/10.1016/s0169-555x(98)00064-6

Duguay, J., Biron, P. M., & Lacey, J. (2022). Impact of density gradients on the secondary flow structure of a river confluence. *Water Resources Research*, *58*(10), e2022WR032720. https://doi.org/10.1029/2022WR032720

Duguay, J. M., Biron, P. M., & Lacey, R. W. J. (2023). Density effects on streamwise-orientated vorticity at river confluences: A laboratory investigation. *Journal of Fluid Mechanics*, *973*, A7. https://doi.org/10.1017/jfm.2023.656

Gaudet, J. M., & Roy, A. G. (1995). Effect of bed morphology on flow mixing length at river confluences. *Nature*, *373*(6510), 138–139. https://doi.org/10.1038/373138a0

Gooseff, M. N., Bencala, K. E., & Wondzell, S. M. (2008). Solute transport along stream and river networks. In A. Roy, S. Rice & B. L. Rhoads (Eds.), *River Confluences, Tributaries and the Fluvial Network* (pp. 395–417). Wiley.

Horna-Munoz, D., Constantinescu, G., Rhoads, B., Lewis, Q., & Sukhodolov, A. (2020). Density effects at a concordant bed natural river confluence. *Water Resources Research*, *56*(4). https://doi.org/10.1029/2019wr026217

Kenworthy, S. T., & Rhoads, B. L. (1995). Hydrologic control of spatial patterns of suspended sediment concentration at a stream confluence. *Journal of Hydrology*, *168*(1–4), 251–263. https://doi.org/10.1016/0022-1694(94)02644-q

Kiffney, P. M., Greene, C. M., Hall, J. E., & Davies, J. R. (2006). Tributary streams create spatial discontinuities in habitat, biological productivity, and diversity in mainstem rivers. *Canadian Journal of Fisheries and Aquatic Sciences*, *63*(11), 2518–2530. https://doi.org/10.1139/f06-138

Lane, S. N., Parsons, D. R., Best, J. L., Orfeo, O., Kostaschuk, R. A., & Hardy, R. J. (2008). Causes of rapid mixing at a junction of two large rivers: Rio Parana and Rio Paraguay, Argentina. *Journal of Geophysical Research*, *113*(F2), F02019. https://doi.org/10.1029/2006jf000745

Laraque, A., Guyot, J. L., & Filizola, N. (2009). Mixing processes in the Amazon River at the confluences of the Negro and Solimoes Rivers, Encontro das Aguas, Manaus, Brazil. *Hydrological Processes*, *23*(22), 3131–3140. https://doi.org/10.1002/hyp.7388

Launay, M., Le Coz, J., Camenen, B., Walter, C., Angot, H., Dramais, G., et al. (2015). Calibrating pollutant dispersion in 1-D hydraulic models of river networks. *Journal of Hydro-Environment Research*, *9*(1), 120–132. https://doi.org/10.1016/j.jher.2014.07.005

Lewis, Q., Rhoads, B., Sukhodolov, A., & Constantinescu, G. (2020). Advective lateral transport of streamwise momentum governs mixing at small river confluences. *Water Resources Research*, *56*(9). https://doi.org/10.1029/2019wr026817

Lewis, Q. W., & Rhoads, B. L. (2015). Rates and patterns of thermal mixing at a small stream confluence under variable incoming flow conditions. *Hydrological Processes*, *29*(20), 4442–4456. https://doi.org/10.1002/hyp.10496

Lyubimova, T. P., Lepikhin, A. P., Parshakova, Y. N., Kolchanov, V. Y., Gualtieri, C., Lane, S., & Roux, B. (2021). Hydrodynamic aspects of confluence of rivers with different water densities. *Journal of Applied Mechanics and Technical Physics*, *62*(7), 1211–1221. https://doi.org/10.1134/S0021894421070130

MacKay, J. R. (1970). Lateral mixing of the Liard and Mackenzie rivers downstream from their confluence. *Canadian Journal of Earth Sciences*, *7*(1), 111–124. https://doi.org/10.1139/e70-008

Matsui, E., Salati, F., Friedman, I., & Brinkman, W. L. F. (1976). Isotopic hydrology in the Amazonia: 2. Relative discharges of the Negro and Solimões rivers through ^{18}O concentrations. *Water Resources Research*, *12*(4), 781–785. https://doi.org/10.1029/WR012i004p00781

Meem, T. H., Rhoads, B., Lewis, Q., Umar, M., & Sukhodolov, A. (2025). Mixing data for 150 mixing events at 43 confluences across the USA [Dataset]. *University of Illinois Urbana-Champaign*. https://doi.org/10.13012/B2IDB-5324086_V1

Pouchoulin, S., Le Coz, J., Mignot, E., Gond, L., & Riviere, N. (2020). Predicting transverse mixing efficiency downstream of a river confluence. *Water Resources Research*, *56*(10). https://doi.org/10.1029/2019wr026367

Ramon, C. L., Armengol, J., Dolz, J., Prats, J., & Rueda, F. J. (2014). Mixing dynamics at the confluence of two large rivers undergoing weak density variations. *Journal of Geophysical Research-Oceans*, *119*(4), 2386–2402. https://doi.org/10.1002/2013jc009488

Rhoads, B. L. (2020). *River dynamics: Geomorphology to support management*. Cambridge University Press.

Rhoads, B. L., & Kenworthy, S. T. (1995). Flow structure at an asymmetrical stream confluence. *Geomorphology*, *11*(4), 273–293. https://doi.org/10.1016/0169-555X(94)00069-4

Rhoads, B. L., & Sukhodolov, A. N. (2001). Field investigation of three-dimensional flow structure at stream confluences: 1. Thermal mixing and time-averaged velocities. *Water Resources Research*, *37*(9), 2393–2410. https://doi.org/10.1029/2001WR000316

Rutherford, J. C. (1994). *River mixing*. Wiley.

Stallard, R. F. (1987). Cross-channel mixing and its effect on sedimentation in the Orinoco River. *Water Resources Research*, *23*(10), 1977–1986. https://doi.org/10.1029/WR023i010p01977

Sukhodolov, A. N., Krick, J., Sukhodolova, T. A., Cheng, Z., Rhoads, B. L., & Constantinescu, G. S. (2017). Turbulent flow structure at a discordant river confluence: Asymmetric jet dynamics with implications for channel morphology. *Journal of Geophysical Research-Earth Surface*, *122*(6), 1278–1293. https://doi.org/10.1002/2016jf004126

Sukhodolov, A. N., & Rhoads, B. L. (2001). Field investigation of three-dimensional flow structure at stream confluences: 2. Turbulence. *Water Resources Research*, *37*(9), 2411–2424. https://doi.org/10.1029/2001WR000317

Sukhodolov, A. N., Schnauder, I., & Uijttewaal, W. S. J. (2010). Dynamics of shallow lateral shear layers: Experimental study in a river with a sandy bed. *Water Resources Research*, *46*(11). https://doi.org/10.1029/2010wr009245

Sukhodolov, A. N., Shumilova, O. O., Constantinescu, G. S., Lewis, Q. W., & Rhoads, B. L. (2023). Mixing dynamics at river confluences governed by intermodal behaviour. *Nature Geoscience*, *16*(1), 89–93. https://doi.org/10.1038/s41561-022-01091-1

Sukhodolov, A. N., & Sukhodolova, T. A. (2019). Dynamics of flow at concordant gravel bed river confluences: Effects of junction angle and momentum flux ratio. *Journal of Geophysical Research-Earth Surface*, *124*(2), 588–615. https://doi.org/10.1029/2018jf004648

Tang, H., Zhang, H., & Yuan, S. (2018). Hydrodynamics and contaminant transport on a degraded bed at a 90-degree channel confluence. *Environmental Fluid Mechanics*, *18*(2), 443–463. https://doi.org/10.1007/s10652-017-9562-8

Tavernini, D. A., & Richardson, J. S. (2020). Effects of tributary size on the resource supply and physical habitat at tributary junctions along two mainstem rivers. *Canadian Journal of Fisheries and Aquatic Sciences*, *77*(8), 1393–1408. https://doi.org/10.1139/cjfas-2019-0435

Umar, M., Rhoads, B. L., & Greenberg, J. A. (2018). Use of multispectral satellite remote sensing to assess mixing of suspended sediment downstream of large river confluences. *Journal of Hydrology*, *556*, 325–338. https://doi.org/10.1016/j.jhydrol.2017.11.026

van Rooijen, E., Mosselman, E., Sloff, K., & Uijttewaal, W. (2020). The effect of small density differences at river confluences. *Water*, *12*(11), 3084. https://doi.org/10.3390/w12113084

Wang, Y., Wang, W., Liu, L., Wang, R., Tang, X., Li, Y., & Li, X. (2024). Spatial heterogeneity of the effects of river network patterns on water quality in highly urbanized city. *Science of the Total Environment*, *937*, 173549. https://doi.org/10.1016/j.scitotenv.2024.173549

Yuan, S., Xu, L., Tang, H., Xiao, Y., & Whittaker, C. (2022). Swimming behavior of juvenile silver carp near the separation zone of a channel confluence. *International Journal of Sediment Research*, *37*(1), 122–127. https://doi.org/10.1016/j.ijsrc.2021.08.002

Zhang, T., Feng, M., & Chen, K. (2023). The quantitative response of pollutant spatial distribution and mixing dynamics to confluent conditions in an asymmetric open-channel confluence. *Journal of Hydrology*, *620*, 129479. https://doi.org/10.1016/j.jhydrol.2023.129479

Zhang, T., Feng, M., Chen, K., & Cai, Y. (2020). Spatiotemporal distributions and mixing dynamics of characteristic contaminants at a large asymmetric confluence in northern China. *Journal of Hydrology*, *591*, 125583. https://doi.org/10.1016/j.jhydrol.2020.125583